Physics – Uspekhi **50** (7) 691 – 704 (2007)

REVIEWS OF TOPICAL PROBLEMS PACS numbers: 61.43.Dq, **61.46. – w**, **61.48. + c**, **81.07. – b**

Hydrogen in nanostructures

R A Andrievski

DOI: 10.1070/PU2007v050n07ABEH006297

Contents

Abstract. The present experimental knowledge of the properties of hydrogen nanostructures is reviewed. The behavior of hydrogen is discussed for nanomaterials made from metals, alloys, intermetallics, and semiconductors (silicon, germanium, etc.), as well as from fullerenes and carbon and other nanotubes. Methods for fabricating nanostructures from these objects are briefly outlined. Structural features, defects, solubility and diffusion mobilities, and thermodynamic and physical properties are discussed. Some aspects still to be clarified are pointed out.

1. Introduction

The increasingly growing interest in nanocrystal materials has been apparent over the last several years due to their remarkable properties, characteristic of the nanostructured state (see, e.g., Refs [1 – 6]). The size effects responsible for the high-level properties are most prominent within the range up to 100 nm. They are determined by at least four causes:

• the role of interfaces substantially increases with decreasing the crystal size (film thickness, nanoparticle and nanowire diameter);

• the characteristics and composition of interfaces in the nanometer range may differ from those of macrocrystals and large-size objects;

• as the size of crystallites decreases, it becomes comparable with characteristic sizes of certain physical phenomena (e.g., free path length of carriers in transport processes);

• finally, quantum effects manifest themselves when the crystal size becomes comparable to the de Broglie wavelength.

All these circumstances affect the potential nonmonotonic process of property changes in the nanometer interval and the occurrence of special points in the property/size dependence for crystals (grains), which are not always possible to predict a priori. Nanomaterials are finding increasingly wider applications, but the problem of realization of optimal nanostructures in terms of maximum exposition of their properties and stability awaits resolution.

It is therefore interesting to consider the specific behavior of hydrogen in nanostructures. Such analysis may be useful from a purely theoretical standpoint (phase diagrams and transitions, diffusion and vibrational spectrum, structural localization and electron state) and for many important applications (solid hydrogen storage systems, electrochemical current sources, sensors, etc.). We emphasize that hydrogen compounds such as hydrides have attracted the attention of researchers since long ago. This interest has been marked by several peaks that emerged from the requirements of atomic technologies [7], constructional physical metallurgy [8], and arising hydrogen energetics [9, 10] on the one hand, and from the necessity to better understand the nature of these typical solutions and introduction phases [9 – 13] on the other hand. The great variety of possibilities offered by nanotechnologies has given a new impetus to the study of hydrogen nanostructures, as evidenced by the large number of conferences and symposia on this issue over the last several years (see, e.g., Refs [14 – 19]), to say nothing about publications in periodicals. This fact and the importance of research in hydrogen energetics and fuel cells [20] prompted the idea of this review.

The division of the objects considered below into metals and intermetallics, semiconductors, and dielectrics is arbitrary and is made for convenience. In the nanocrystalline state, the situation may be quite different, e.g., in the case of various transport characteristics of carriers in carbon nanotubes (many authors regard even fullerenes as semicon-

R A Andrievski Institute of Problems of Chemical Physics,
Russian Academy of Sciences,
prosp. akad. Semenova 1, 142432 Chernogolovka, Moscow region,
Russian Federation
Tel./Fax (7-496) 522 35 77
E-mail: ara@icp.ac.ru

Received 27 November 2006, revised 26 February 2007
Uspekhi Fizicheskikh Nauk **177** (7) 721 – 735 (2007)
Translated by Yu V Morozov; edited by A M Semikhatov

ductors). We consider the synthesis of hydrogen nanostructures only in general outline because this problem requires special analysis, and focus attention on the structure and properties of these materials.

2. Metals and intermetallics

2.1 Fabrication methods

Practically all methods of manufacturing hydrogen nanostructures are based on saturation of powders and films with hydrogen. For hydride nanostructural phases, Refs [21, 22] demonstrated the advantages of high-energy grinding as a method for fabricating highly dispersed powders of hydride-forming intermetallics like Mg_2Ni from the starting metallic components (the so-called mechanosynthesis). Powders thus obtained absorbed hydrogen and formed the compound Mg_2NiH_4 (which is close to stoichiometric) several times quicker than ordinary objects (pieces of melted intermetallics) [22]. The proposed method of mechanosynthesis immediately gained popularity especially in application to poorly hydrated alloys and magnesium-based compounds, as well as for the introduction of catalyzers, such as palladium, graphite, etc., into hydrated objects. Interest in magnesium hydride is quite understandable because it contains much hydrogen (7.66 mass%). But the kinetic characteristics of magnesium saturation with hydrogen and hydrogen desorption from the hydride need substantial modification to be suitable for practical purposes.

In Table 1, we list hydrides manufactured by mechanical synthesis using high-energy grinding. Only a small number of publications are included whose authors mention the size of the crystals (grains). Nanocrystallicity manifests itself as a considerable increase in hydrogen sorption and desorption rates and a significant decrease in temperature at the beginning of these processes. It was found in Ref. [26] that the size of MgH_2 particles has greater effect on hydrogen desorption than the crystallite size. Probably, an unstable variety of magnesium hydride (γ-MgH_2) formed in the course of grinding and the presence of an oxide film also affect liberation of hydrogen, thus adding uncertainty regarding the role of particle and crystal size in sorption and desorption processes. Certainly, the introduced catalyzers also exert some influence. On the whole, the sorption/desorption activation mechanism and the problem of discrimination between the role of different factors (increased surface and defectiveness, intermediate reactions, dissociation of molecular hydrogen, etc.) remain to be clarified.

We emphasize that the maximum hydrogen content in synthesized nanohydrates is somewhat lower than in the same ordinary phases. Possible causes are discussed in Section 2.3. The search for new alloys, compounds, and composites able to accumulate hydrogen is underway (see, e.g., [14, 16 – 19]); researchers show interest not only in traditional 'metallic' hydrides but also in objects such as alanates, compounds of lithium, borhydrides, and some organic substances. An interesting method for manufacturing layered composites in the $Mg-Ni-Mg_2Ni$ system by combined cold rolling with subsequent thermal treatment and saturation with hydrogen was proposed in Ref. [27]. As the method is gradually improved in application to nanocomposites, it may open up new possibilities for manufacturing hydrogen-accumulating nanohydrides, not only in the form of powders but also as compact multilayer bands, briquettes, etc.

Increasingly more interest in recent years has been shown in hydride films. Early works were episodic (see, e.g., Refs [28 – 30]), but now this problem is the focus of conferences and publications. On the one hand, this is because such films are representative of characteristic model nanomaterials. On the other hand, they are promising for use in sensor devices [31 – 33]. Most results were realized using films based on the classical systems of $Pd-H_2$ [33 – 35] and $Nb-H_2$, although other subjects like monolayer magnesium films [36] and multilayer MmM_5-Mg films (*Mm* is a misch metal or alloy of the most widespread rare earth metals and *M* is a metal) [32] have begun to be equally widely used.

Worthy of mention are the following methods of manufacturing metallic nanopowders and clusters for their subsequent saturation with hydrogen and fabrication of nanohydrides: palladium condensation in an inert medium [3] (used since a long time ago), electrochemical production of palladium clusters with stabilization of their surface by a water-permeable polymer film [37], and synthesis of magnesium hydride by sputtering magnesium in a hydrogen arc plasma [38].

Table 1. Some nanocrystalline hydrides and their fabrication procedures.

Starting components (intermetallic, alloy)	Treatment regime	*L*, *D*, nm	Hydride and saturation conditions	References
$Mg + Ni$	$m = 5$, $t = 60$	$L = 20-30$	$Mg_2NiH_{\sim 0.97}$ $P_{H_2} = 1$, $T = 300\,^\circ C$	[22]
(Mg_2Ni)	$m = 10$, $t = 48$	$L < 15-20$	$Mg_2NiH_{\sim 0.81}$ $P_{H_2} = 1$, $T = 200\,^\circ C$	[23]
$Mg + Ni + Al$ ($Mg_{87}Ni_{10}Al_3$)	$m = 15$, $t = 20$ Grinding in hydrogen	$L \sim 8$	$Mg_2NiH_{\sim 0.81}$ $Mg_2NiH_{\sim 4}$ (traces) $P_{H_2} = 0.6$	[24]
MgH_2 $MgH_2 + 2\%Nb_2O_5$	$m = 10$, $t = 200$	$L \sim 8.5$ $L \sim 7$	$MgH_{\sim 0.98}$ $MgH_{\sim 0.85}$ $P_{H_2} = 1$, $T = 300\,^\circ C$	[25]
MgH_2	$m = 40$, $t = 1-100$ Grinding in hydrogen	$L = 3-60$ $D = 600-1000$	β-$MgH_{\sim 2}$, γ-$MgH_{\sim 2}$ $P_{H_2} \sim 0.7$	[26]

Note. *m* is the mass ratio of the ball and the ground mixture; *L* and *D* are the respective sizes of crystallites and powder particles; *t* is the duration of grinding, h; P_{H_2} is the hydrogen pressure, MPa.

2.2 Structural features

It is easy to demonstrate that the fraction of interfaces with an amorphous structure in a polycrystalline sample is approximately $3s/L$, where s is the width of the borderline region (ca. 1 nm) and L is the grain (crystallite) size. The fraction is estimated to constitute several percent when the grain size does not exceed 100 nm, but amounts to 50% at $L \sim 6$ nm. It is generally accepted that nanostructures resemble amorphous phases in many respects and form a general class of so-called disordered objects. As regards nanostructures, it is essential to clarify whether hydrogen localization changes in the initial crystalline phase proper (i.e., inside nanograins), to what extent borderline regions (interfaces) are enriched in hydrogen, and what defects these objects have. These data are rather scarce and highly scattered.

Neutron structural studies of $FeTiD_{0.97}$ (grain size 10 nm) showed that about 50% of the deuterium atoms are localized at the grain boundaries, where they occupy tetrahedral positions close to titanium atoms (tetrahedrons 4Ti and 3Ti + 1Fe). Deuterium retains its usual octahedral localization inside grain bodies [39]. A comparative neutron structural study of an iron-terbium deuteride $TbFe_2D_{3-3.8}$ in nanocrystalline and amorphous states demonstrated that deuterium atoms are localized in tetrahedrons of the 2Tb + 2Fe type in the former case and in terbium tetrahedrons in the latter [40].

Investigations into inelastic neutron scattering also provide interesting information about localization of hydrogen atoms in hydrides. Figure 1 presents phonon spectra of TiCuH in nanocrystalline and amorphous states [41]. The essential difference between these spectra is quite obvious. When maximum peak energies are identical, the wider peak of the amorphous object may indicate marked deformity of hydrogen tetrahedral positions and atomic fluctuations in their immediate proximity. The shape of the left wing of the peak may reflect the presence of hydrogen atoms in octahedral positions.

NMR spectra of nanocrystalline $PdH_{0.72}$ (grain size 10 nm) exhibit two well-resolvable signals (Fig. 2), suggesting the presence of hydrogen atoms inside grains and at their boundaries at the ratio 1 : 2 [42].

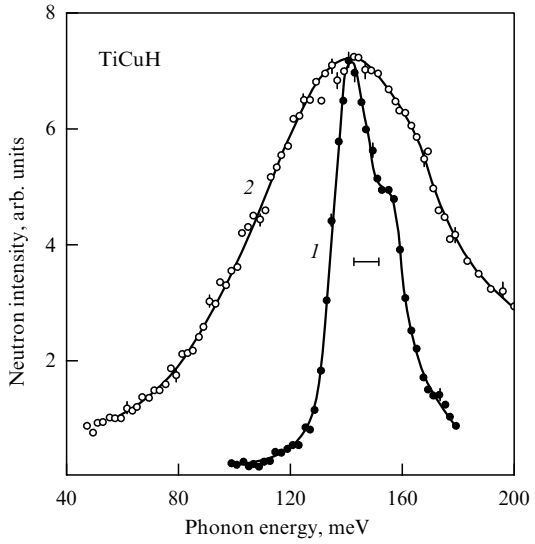

Figure 1. Spectra of neutrons scattered on crystalline $TiCuH_{0.93}$ (*1*) and amorphous $TiCuH_{1.3}$ (*2*) at $T = 78$ K [41].

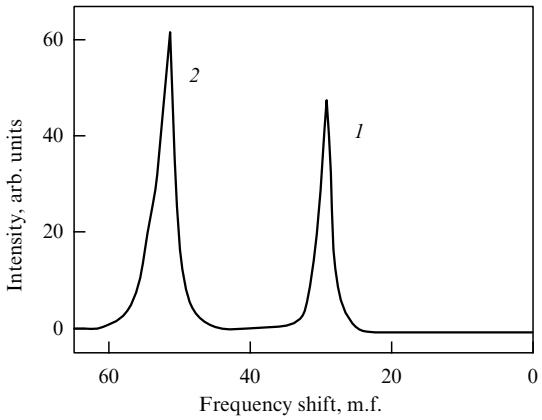

Figure 2. NMR spectrum (frequency 200 MHz) of nanohydride $PdH_{0.72}$: *1* — peak corresponding to hydrogen atoms in the lattice, *2* — peak corresponding to hydrogen atoms on the interface [42].

It is convenient to analyze structural defects using magnesium-based hydrides as an example. Paper [43] reports the results of thorough investigations of the structure and composition of nanocomposites Mg–Ni, Mg–Ni–La, Mg–Ni–Ce, and Mg–$LaNi_5$ obtained by mechanosynthesis. The authors observed amorphization of the nickel phase enveloping progressively diminishing Mg grains in a nanocomposite Mg – 50 mass% Ni.

Duration of grinding t, h	10	20	30	40	50	60
Grain size of Mg, nm	26	18.5	13	12.5	(12.1)	(12)

X-ray structural analysis (XSA) and electron microscopy showed that grinding for 50 hours yielded a completely amorphous nanocomposite (Bragg lines on diffractograms turned into diffusion humps). The sorption/desorption characteristics changed accordingly: the maximum hydrogen absorption was 5.9 mass% at 300 °C and the hydrogen pressure 3 MPa for the grinding duration 30 h and only ~ 1.8 mass% for $t = 50$ h.

The addition of cerium and especially lanthanum or $LaNi_5$ to a Mg–Ni nanocomposite significantly reduced the starting hydrogen absorption/desorption temperature down to ambient values and improved kinetics of these processes but simultaneously decreased the amount of absorbed hydrogen (its content in cerium, lanthanum and $LaNi_5$ hydrides was much lower than in MgH_2; for example, it was only 1.49 mass% H in $LaNi_5H_{6.5}$). The distribution of nickel and lanthanum at the surface of magnesium particles was sometimes inconsistent with the presence of $LaNi_5$; this suggests a decay of this phase in the course of combined grinding. Destructurization of $LaNi_5$ films with the possible formation of nickel clusters was also observed during electrochemical activation [30].

Studies of multilayer MmM_5–Mg films obtained by the magnetron sputtering technique revealed interesting structural features [32]. The total film length was 3100 nm, including 500 nm of Mg and 400 nm of MmM_5. High-resolution transmission electron microscopy (HRTEM) demonstrated the presence of 3–10 nm nanocrystals in MmM_5 layers and a 4 nm thick amorphous interlayer at the boundaries. The magnesium film had a column structure with texture $\langle 001 \rangle$ and chaotically oriented nanocrystals measuring about 50 nm. A schematic of three film layers

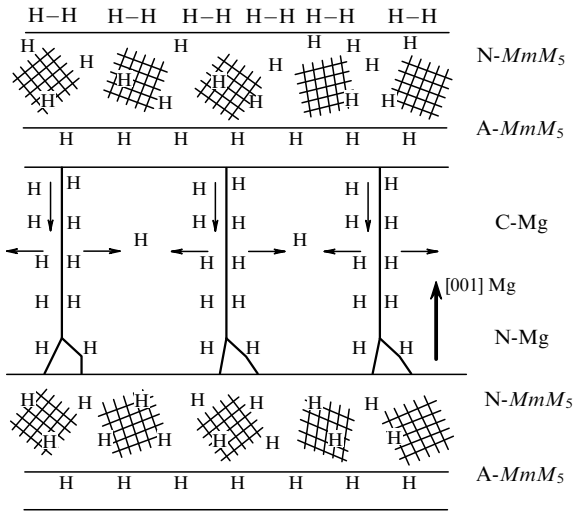

Figure 3. Schematic representation of layers in a hydrated MmM_5/Mg film (H–H and H are molecular and atomic hydrogen; thin arrows indicate hydrogen diffusion at grain boundaries and in the bulk): N-MmMg$_5$ — nanograins in MmMg$_5$; A-MmMg$_5$ — amorphous interlayer of MmMg$_5$; C-Mg — column structure of macrocrystalline Mg with texture $\langle 001 \rangle$; N-Mg — inclusions of Mg grains [32].

(MmM_5–Mg–MmM_5) based on electron microscopic images is presented in Fig. 3.

A post-hydration X-ray structural study of intermetallic Mg_2Ni (grain size less than 15–20 nm) revealed a large number of microtwins attributable to dislocations and other defects that developed during mechanosynthesis [23].

The defects arising from hydration and dehydration of ordinary intermetallic $LaNi_5$ powders have been investigated for more than 10 years [44, 45]. HRTEM and microdiffraction techniques, conventional and scanning electron microscopy (SEM), and energodispersion analysis at different hydration/dehydration stages have allowed a variety of defects to be identified, viz. different types of wall-associated dislocations, misfit and antiphase boundaries, microtwins, structural disorder, and planar defects. Metallic nickel and lanthanum oxide (or $La(OH)_3$) were located at the particle surface. An X-ray study of defects in deformed and annealed commercial powders of $Mm(Ni, Mn, Al, Co)_{5.2}$ ($CaCu_5$-type lattice) was undertaken in Ref. [46].

It can be seen from Table 2, presenting results of this study, that an increase in the grinding duration leads to a significant increase in the period c and, accordingly, the cell volume V. They acquire the initial values after annealing and even slightly decrease, possibly due to atom exchange in sublattices of the $CaCu_5$ structure. At a grinding length below 200 min, plastic deformation plays an increasingly greater role in the reduction of grain size; thereafter, grinding is accompanied by peculiar 'cold welding' of ground particles, stabilization of the grain size ($L = 5$–6 nm), and a substantial increase in the amount of the amorphous phase; it disappears after annealing at a temperature in excess of 400 °C. Characteristically, the degree of lattice deformity alters considerably at the above grinding duration and annealing temperature.

Interactions of hydrogen with nanometals are known better than with intermetallics. These are primarily diluted hydrogen solutions in palladium, niobium, vanadium, and some other metals in the form of thin monolayer films, sometimes clusters and two-layer films. The results of these studies, first and foremost with respect to systems such as Pd–H_2 and Nb–H_2, are described at length in [47, 48]. The main conclusions are as follows:

• analysis of the most reliable data on hydrogen solubility and diffusion in deformed and annealed palladium (as well as electroconductivity parameters of these samples) has demonstrated that dislocations lead to hydride-like nanometer segregations [47];

• hydrogen dissolution in films of Pd, Nb, Y, and other metals with the thickness up to approximately 200 nm causes appreciable compressive stresses, whose absolute value shows a practically linear dependence on the hydrogen concentration in a wide range of compositions of diluted solid solutions (including $MH_{0.08-0.10}$ and $YH_{0.15}$ for yttrium).These results are numerically described in the elastic approximation. A further slowdown in stress enhancement is attributable to relaxation processes and the generation and motion of dislocations [48];

• the structural evolution of thin films hydrated on substrates depends on the relation between the physicomechanical properties and thickness of these objects. It has been most thoroughly studied in the Nb–H_2 system (film thickness up to 200 nm, crystallite size 7–17 nm, sapphire, quartz and silicon substrates). Atomic-force and scanning tunnel microscopy (AFM and STM) revealed significant changes in the morphological structure and composition of a metallic film surface following hydration. Specifically, column hydride structures several nanometers in height were observed to appear [48]. This finding agrees with the earlier data for a Pd–H_2 system [47].

Table 2. Periods and volume of an elementary cell (a, c, and V), grain size and lattice deformation (L and ε) in intermetallic $Mm(Ni, Mn, Al, Co)_{5.2}$ after grinding ($m = 10$) and annealing (after grinding for 3000 min) in an Ar medium ($t = 1.5$ h) [46].

Treatment	a, nm	c, nm	V, nm^3	L, nm	ε, %	Amorphous phase, %
Initial state	0.498626	0.405526	0.087317	54 ± 5	0.004	—
Grinding, 7 min	0.49867	0.40551	0.087329	42 ± 4	0.014	—
Grinding, 15 min	0.49866	0.40570	0.08736	13.5 ± 2	0.26	~ 5
Grinding, 45 min	0.49842	0.40570	0.08728	14 ± 2	0.12	10
Grinding, 200 min	0.4981	0.4084	0.08775	5.8 ± 1.7	0.62	25
Grinding, 1000 min	0.4993	0.4130	0.0892	5 ± 2	0.63	35
Grinding, 3000 min	0.4979	0.4158	0.0893	5 ± 3	0.5	45
Annealing, 175 °C	0.4976	0.4089	0.08768	7.2 ± 4	0.84	30
Annealing, 330 °C	0.4968	0.4090	0.08742	10 ± 1	0.77	~ 15
Annealing, 400 °C	0.49699	0.40610	0.08687	16 ± 6	0.65	—
Annealing, 550 °C	0.49852	0.40278	0.86689	37 ± 4	0.16	—

The above results are helpful in interpreting the effect of nanocrystallicity on metal–hydrogen phase diagrams (see Figs 4–6 below).

2.3 Solubility and diffusion mobility

Figures 4–6 show hydrogen solubility isotherms in intermetallics FeTi and MmM_5 and in palladium with different grain sizes [46, 49, 50]. Solubility obviously increases in solid nanocrystalline solutions and especially in amorphous samples. Similar results were obtained for thin films of hydride systems $d-H_2$ and $Nb-H_2$ [48]. Specifically, for 200 nm thick large-grained Nb films, the maximum hydrogen solubility in a solid solution and the minimum solubility in the adjacent hydride phase are $C_{\alpha H} = 0.06\,H/Nb$ and $C_{\beta H} = 0.70\,H/Nb$, respectively (in agreement with the data for ordinary nacrocrystalline samples; here, α is a solid hydrogen solution in the metal and β is the hydride phase). These values are significantly different for 25 nm thick films with the grain size ~ 10 nm ($C_{\alpha H} = 0.37\,H/Nb$ and $C_{\beta H} = 0.64\,H/Nb$).

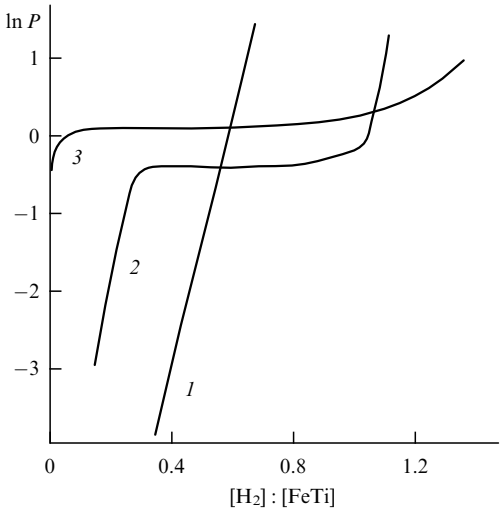

Figure 4. Isotherms of hydrogen sorption by intermetallic FeTi ($T = 293$ K): *1* — amorphous sample, *2* — nanocrystalline sample (grain size ~ 5 nm), *3* — macrocrystalline sample [49].

As noted above, the results of neutron structural analysis and NMR studies (see Fig. 2) [39, 42] taken together with the above data on hydride films [47, 48] suggest high hydrogen content on grain boundaries; in other words, interfaces are responsible for the general enhancement of solubility. High solubility in amorphous objects is related to the absence of a long-range order and, accordingly, to a large number of suitable positions for hydrogen atoms (see Fig. 1) [41].

Figures 4–6 show a two-phase region on the diagrams for $FeTi-H_2$, MmM_5-H_2, and $Pd-H_2$, known to have constant hydrogen pressure and to be determined by the size of the plateau in the dependence $P_{H_2} = f(H/M)$. It narrows in nanocrystalline samples and disappears in amorphous samples of FeTi and MmM_5. A similar narrowing of two-phase regions was reported for a $Pd-H_2$ system during transition from ordinary powders to nanoparticles measuring 6 and 3 nm [37], the $LaNi_5-H_2$ system in the course of intermetallic grinding [51], and nanocrystalline films in a $Nb-H_2$ system [48].

The possibility of narrowing the biphasic region during contact between the saturated α-phase and the metastable β-phase was demonstrated and analyzed in the well-known monograph [52]. The author arrived at the conclusion that the solubility of metastable phases is always higher than that of stable (steady-state) phases. In the cases under consideration, metastable phases are understood as hydride segregations at interfaces and dislocations observed in many studies [47, 48].

It follows from experimental data for $Pd-H_2$ systems that the disintegration temperature T_c (or the maximum temperature for the existence of the two-phase region) in ordinary and nanocrystalline palladium is 570 and 435 K, respectively. Rather simple transformations of the expression for hydrogen activity in the solid phase written with the help of the conventional quasi-chemical approximation for regular solutions lead to the conclusion that transition to the nanocrystalline state is accompanied by an almost 20% decrease in the mixing energy [50]. The effect of the epitaxial film thickness on T_c was also elucidated in many $Nb-H_2$ studies; but a stress-related contribution needs to be taken into consideration in the case of film samples [48].

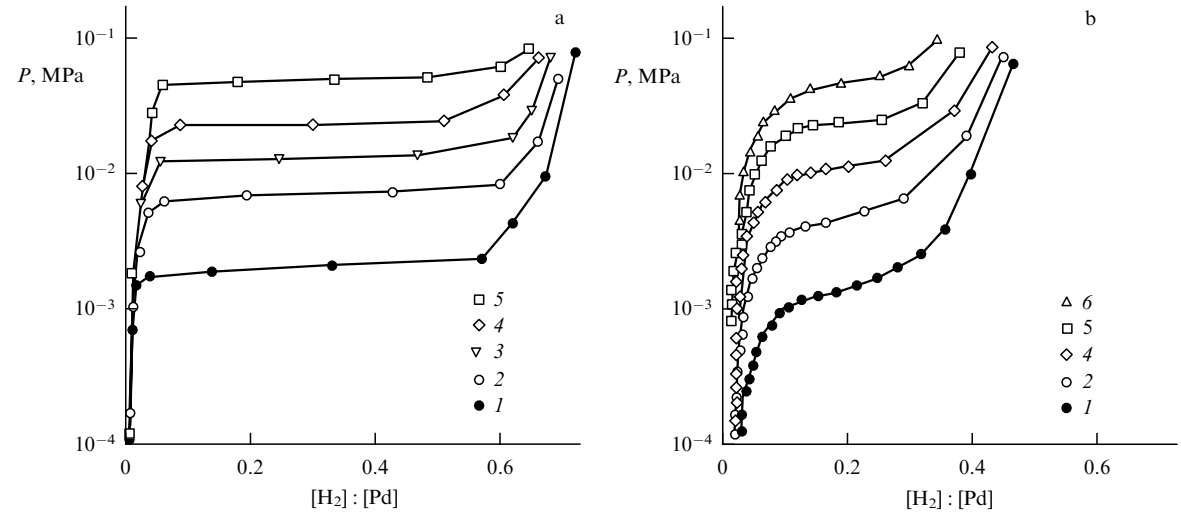

Figure 5. Isotherms of hydrogen sorption by macrocrystalline (a) and nanocrystalline (grain size ~ 10 nm) (b) palladium at different temperatures: (*1*) 298, (*2*) 323, (*3*) 338, (*4*) 353, (*5*) 373, (*6*) 398 K [50].

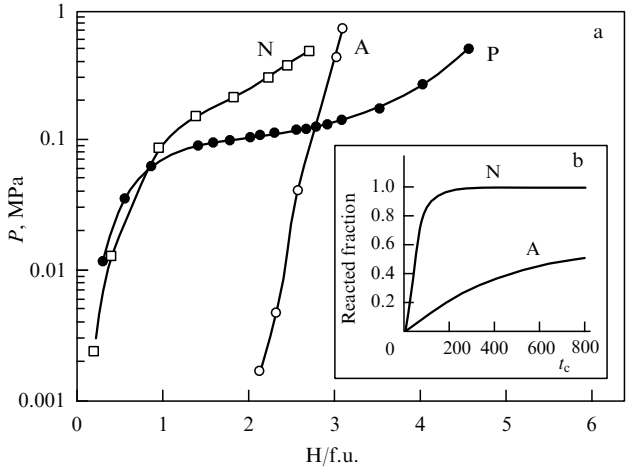

Figure 6. Isotherms (a) and kinetics (b) of hydrogen sorption by intermetallic $MmM_{5.2}$ at 328 K (hydrogen pressure 1 MPa): A — sample after grinding for 3000 min (amorphous phase content 45%), P — starting sample (grain size $\sim$ 54 nm), N — sample after grinding and annealing at 673 K (grain size $\sim$ 16 nm). Sample characteristics are specified in Table 2 [46].

The data in Table 1 and Figs 4–6 indicate that the maximum hydrogen content in nano- and amorphohydrides is lower than in ordinary hydrides of the same composition. These objects also differ in terms of dissociation pressure. The maximum content of hydrogen in palladium hydride films is also reduced ($PdH_{\sim 0.67}$, the film thickness on the magnesium substrate $\sim$ 30 nm) [35]. As is known, a change in the dissociation pressure in the hydride homogeneity region can be described in the framework of the local configuration approximation [10, 12]. It may be conjectured that numerous defects in nano- and amorphohydrides block some potential positions of hydrogen atoms and decrease the configuration entropy; as a result, the dissociation pressure increases. Comparison of hydrogen absorption kinetics in nanocrystalline (N) and amorphous (A) samples in Fig. 6b indicates that diffusion mobility is significantly smaller in the latter. Similar data were obtained in an earlier study of amorphous and nanocrystalline composites Mg–Ni [43].

The problem of hydrogen interaction with amorphous alloys and hydrogen diffusion in disordered metals and alloys has been thoroughly analyzed in Refs [53, 54]. Hydrogen was found to be highly soluble in these objects and its behavior exhibited a strong concentration dependence. Various theoretical approaches are largely based on the models that postulate a wide distribution of positions for hydrogen atoms in the systems of interest. Hydrogen diffusion in disordered objects is characterized by deviation of the temperature-dependent alteration of the diffusion coefficient from the conventional Arrhenius function. For example, the hydrogen self-diffusion activation energy in amorphous $TiCuH_{1.4}$ is described by the following parameters:

Temperature range, K	139 – 208	208 – 340	340 – 417
Activation energy, eV	0.089	0.22	0.47

At the same time, the activation energy in crystalline $TiCuH_{0.94}$ is constant (0.87 eV) [53], and hence the ratios of the absolute hydrogen diffusion coefficients in amorphous and crystalline objects are different in different temperature ranges.

Nonmonotonic concentration-dependent variations of the hydrogen diffusion coefficient in nanocrystalline palladium were described long ago [55]. Peculiarities of hydrogen diffusion in disordered objects were attributed to the presence of a variety of energy positions. In [56], hydrogen diffusion in nanometals was considered using a two-phase model (crystalline matrix and grain boundaries) with two types of interstitial sites. The obtained expressions allow the general analysis of different variants with the concentration, correlation, and other effects taken into account. The notion of hydrogen segregations along dislocations proved instrumental in the analysis of the chemical diffusion of hydrogen (i.e., with reference to its gradient) in deformed and annealed palladium samples [47].

Evaluation of the hydrogen permeability of multilayer nanostructured Pd/Fe and Pd/Ni films demonstrated that the permeability obeyed the known Sievert law ($P^{0.5}$ proportionality) regardless of the increase in the number of interphase interfaces [57]. But comparison of experimental data with calculations based on tabulated data for bulk Pd, Fe, and Ni samples revealed different behavior for Pd/Fe and Pd/Ni films. In the former case, experimental results were below and in the latter case above the theoretical ones. The authors of Ref. [57] attributed this difference to the possible presence of dislocations in the iron layers that facilitated 'entanglement' of hydrogen atoms and a decrease in the grain size in the nickel layers. Taken together, these factors increased the contribution of boundary diffusion to the total diffusion flow. However, structural information presented in Ref. [57] is undetailed and insufficient.

2.4 Physical properties

The remarkable possibility to observe metal–dihydride–trihydride conversions accompanied by a striking alteration of electric and optic properties (from metals to semiconductors, from reflection to transmission of visible light) was demonstrated using hydrogen-permeable yttrium and lanthanum films preventing oxidation [58]. Synthesis of thin hydride films was combined with investigation of their electrical properties in systems $LaNi_5-H_2$, $MmNi_{4.5}-H_2$, $LaCo_5-H_2$, FeTi–H_2, FeTiMn–H_2, Pd–H_2, and Mg–H_2 (see, e.g., Refs [28, 34, 36, 59–61]). Measurements (especially in earlier studies) were complicated by potential oxidation and the formation of oxides and other phases. The recent, most representative data suggest that hydration of intermetallics enhances their resistivity (by approximately 20% for RNi_5, where R is a rare earth element, and several-fold for FeTi). Vice versa, dehydration decreases the resistivity.

Halvanomagnetic measurements yielded interesting results that allowed evaluating both the concentration (10^{19} cm^{-3}) and the sign of carriers in intermetallics and intermetallic-based hydride phases from the Hall coefficient values in the framework of the single-band model [61].

	$LaNi_5$	FeTi
Before hydration	−0.58	−0.042
After hydration	+0.5	+7.17

A similar reversal of the sign of the Hall coefficient during hydration of FeTi and FeTiMn was observed in Ref. [60],

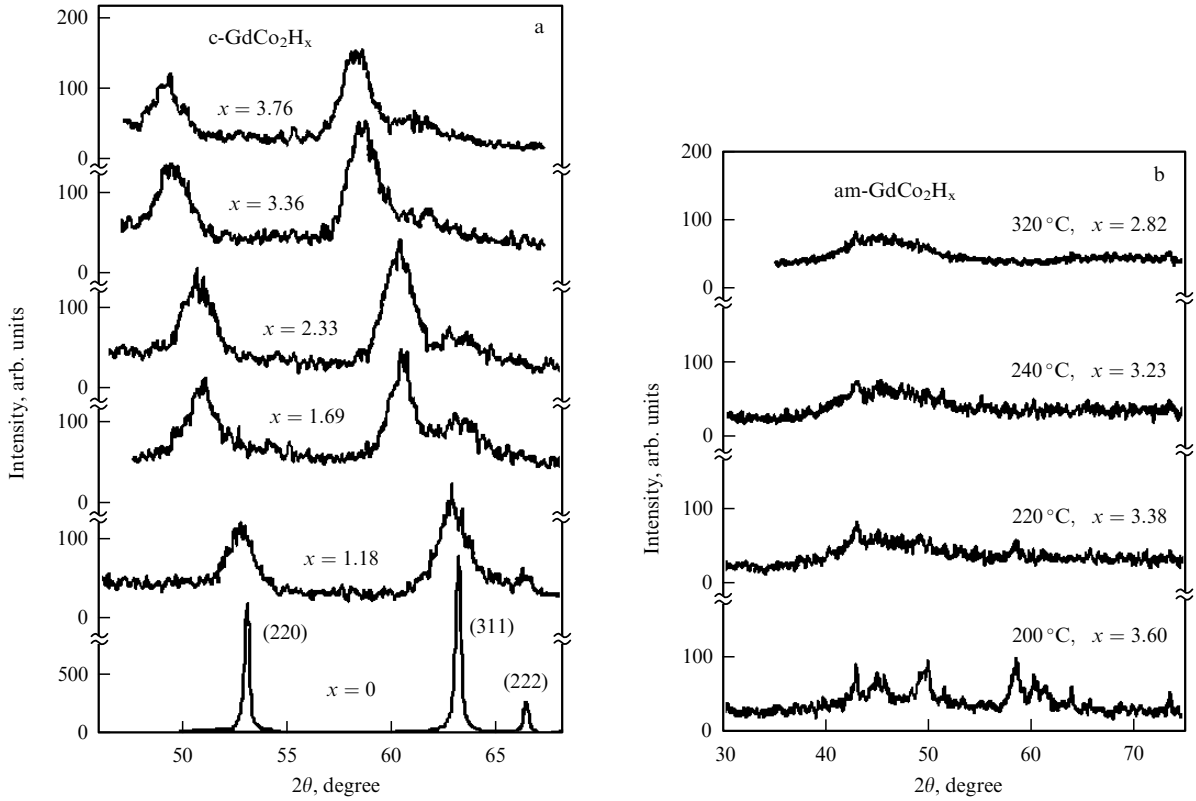

Figure 7. Diffractograms of $GdCo_2$ samples containing different amounts of hydrogen: (a) crystalline state, (b) amorphous state; x is the formula ratio in $GdCo_2H_x$ [64].

although absolute concentrations of electrons and holes were different, viz. roughly -3×10^{19} cm^{-3} for FeTi and $+30 \times 10^{19}$ cm^{-3} for $FeTiH_x$. The quantitative difference between the results reported in Refs [60, 61] was most likely due to uncontrolled hydrogen and oxygen content in the films.

Many researchers interpret the difference in the character of carriers in hydrides and starting intermetallics as resulting from the capture of electrons by hydrogen atoms from an sd-hybrid metallic band and as evidence of the anyonic nature of hydrides. The problem of electronic structure of hydrides is known to have a long history (see, e.g., Refs [9–12]). Reversal of the sign of the Hall coefficient occurs in the homogeneity region of zirconium hydride having an undoubtedly metal-like nature [10, 12]. In other words, arguments about the ionic character of $LaNi_5$- and FeTi-based nanohydrides cannot be implicitly accepted and need to be verified in further studies, such as evaluation of the temperature-dependent resistivity.

A thorough study of the electric and optical properties of thin PdH films on different substrates (In–Sn oxide, glass, dysprosium film) was undertaken in [34]. It was shown that the transmission of visible light by 19 nm thick Pd films increased as the hydrogen concentration increased, the increase being especially pronounced starting from compositions such as $PdH_{0.6}$ on metallic substrates. The film resistivity increased insignificantly as the hydrogen concentration increased; simultaneously, the concentration of carriers and the state density at the Fermi level decreased. The free path length of electrons was ~ 10 nm, i.e., 2.5 times lower than in bulk palladium.

The above peculiarities of the effect of hydrogen on the electron properties of thin (nanostructured) palladium hydride films are on the whole analogous to the characteristics of ordinary palladium hydride [9, 11, 13]. Certainly, further thorough measurements of the electron heat capacity, low-temperature magnetic susceptibility, and superconductivity are needed to deeper understand the electron structure of PdH in the nanocrystalline state. Such data may have practical implications, besides theoretical interest, because Pd films are used to protect switchable mirror films of rare-earth metals (REMs) and in optoelectronic devices. Factors influencing the stability of metallohydride switchable mirror devices [multilayer $Pd/Mg_x(Mn_{0.75}Ni_{0.25})_{1-x}$-based films] have been considered in [62].

Hydrogen saturation of many intermetallics based on REMs and transition metals (of the R_nM_m type, where R is Y, La, Gd, Tb, Dy, Lu, Ho, or Er and M is Fe, Co, Ni, or Mn) leads to amorphization and noticeable alteration of magnetic properties (see [63]). The magnetic properties of intermetallics are known to be formed by two magnetic subsystems of 4f- and 3d-metals. Such compounds belong to the so-called two-sublattice ferrimagnetics. It is believed that hydration results in the weakening of $R-M$ exchange interactions. The effect of hydrogen is conveniently observed in intermetallic $GdCo_2$. Figure 7 presents diffractograms of hydride intermetallics of different composition in crystalline and amorphous states [64]. It can be seen that hydration up to a maximum ($x = 3.76$) does not produce a new phase; all hydride compounds are isostructural to the starting intermetallic $GdCo_2$ (cubic structure of the $MgCu_2$-type), but reflexes broaden considerably and shift towards smaller angles. The elementary cell has a larger volume (especially for $x > 1.6$) due to the invasion of tetrahedron positions by hydrogen atoms (Fig. 7a). Broadening of reflexes is indicative not only of decreased grain size but also of lattice micro-

distortions. Unfortunately, the authors of Ref. [64] did not differentiate between these effects. Nevertheless, examination of magnetic properties revealed a substantial decrease in the magnetic moment in Co and the magnetic ordering temperature as a result of structural disintegration.

Amorphization of the structure, apparent as a wide halo in diffractograms (Fig. 7b), occurred during hydration at 490 – 590 K. Heating above 590 K caused disintegration of the hydride intermetallic and liberation of gadolinium and cobalt. Amorphous hydride phases behaved like ferrimagnetics. Evaluation of temperature-dependent variations in the magnetic moments of these phases showed that the compensation temperature decreased with increasing the amorphization temperature (decreasing the hydrogen concentration); this suggested a weakening of the Gd – Co exchange interaction.

A study of damping characteristics of nanostructured quasi-crystals of Zr – Cu – Ni – Al and Ti – Zr – Ni demonstrated that relaxation peaks changed significantly under the effect of hydrogen; their broadening and heightening evidenced structural amorphization [65].

3. Semiconductors

3.1 Fabrication methods and structural features

Interest in hydrogen-containing semiconducting nanostructures was stimulated by the discovery of photoconductivity in films of amorphous hydrated silicon (a-Si:H) and the possibility of their diverse applications in photoreceiving devices, including solar cells. Further studies showed that under certain conditions these objects may contain inclusions of nanocrystalline silicon contributing to their photosensitivity and stability (see, e.g., Refs [66 – 68]). There are several methods for manufacturing nanocomposites of the nc-Si/(a-Si:H)-type, such as precipitation from a silane glow-discharge plasma in various forms (continuous, cyclic, with intermediate annealing, etc.), high-frequency and arc-discharge sputtering, and H^+ and Si^+ implantation.

Evidently, Si nanocrystals in the amorphous silicon matrix form under far-from-equilibrium conditions. Investigations of the mechanism of this process and its dependence on the temperature, hydrogen content, film defects, plasma composition, implantation doses, and other factors are underway.

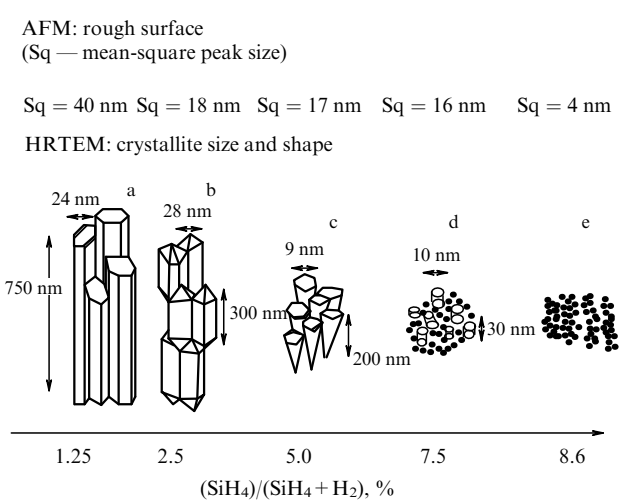

Figure 8. Schematic of the structures realized in silane plasma of various compositions: $(SiH_4)/(SiH_4 + H_2)$: (a) 1.25, (b) 2.5, (c) 5, (d) 7, (e) 8.6% [69].

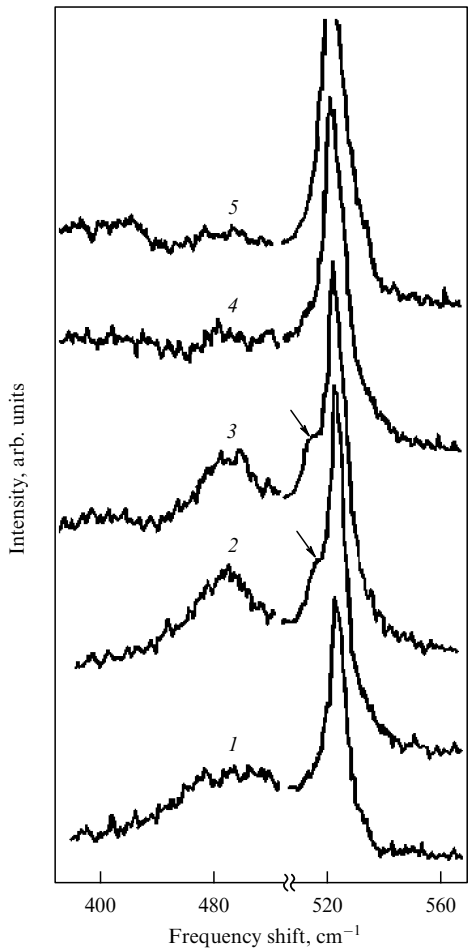

Figure 9. CS spectra of H^+ ion-doped silicon samples with the energy 24 keV at 3×10^{17} cm^{-2} prior to annealing (*1*) and after 10 s of annealing at $T = 573$ (*2*), 673 (*3*), 873 (*4*), and 973 K (*5*) [71].

Figure 8, based on AFM and HRTEM data, schematically depicts the evolution of the microstructure of the layers precipitated in a high-frequency glow-discharge plasma (70 MHz, 7 W) at different silane concentrations [69]. It can be seen that the addition of silane has a dramatic effect on the morphology (including surface roughness), size, and phase composition of the resulting products. Concentration variants a – c reflect the structure of nanocrystalline films, variant d corresponds to composite nc-Si/a-Si and variant e to amorphous silicon. A detailed study of the effect of these structural patterns on transport properties (dark conductivity, photoconductivity, diffusion length of charge carriers, etc.) is reported in Ref. [70].

Implantation of H^+ ions results in nano- and micropores that coalesce in the course of annealing and accumulate molecular hydrogen. Formation of nanocrystals depends on the hydrogen content; it is estimated [71] that active crystallization occurs at the hydrogen content above 20 at.%. HRTEM analysis of combination light scattering (CS) and photoluminescence spectra showed that implantation of large doses of H^+ ions (10^{17} and 3×10^{18} cm^{-2}, energy 24 keV) causes nanocrystals in silicon layers on an dielectric to form in the amorphous matrix after short-term annealing starting from 300 °C [71]. Figure 9 shows CS spectra before and after

annealing at different temperatures. The broad peak with the maximum near 480 cm^{-1} coincides with the spectrum of amorphous silicon and corresponds to the amorphous component. The peak at 520 cm^{-1} is related to scattering on silicon optical phonons and corresponds to the silicon matrix. Finally, the peak at 490 – 500 cm^{-1} that appears after annealing (arrow) is believed to correspond to nanocrystals formed in the silicon matrix. Some authors propose assessing the volume fraction of nanocrystals in the amorphous matrix (F_{cr}) and the interface fraction (F_{gb}) from the analysis of CS spectra using the relations

$$F_{cr} = \frac{I_{cr} + I_{gb}}{I_{cr} + I_{gb} + y(L)I_a}$$

and

$$F_{gb} = \frac{I_{gb}}{I_{cr} + I_{gb} + y(L)I_a},$$

where I_{cr}, I_{gb}, and I_a are the respective peak intensities of the silicon matrix, nanocrystals, and amorphous component and $y(L) = 0.1 + \exp(-L/L_0)$ is a function depending on the grain size L ($L_0 = 25$ nm) [72, 73]. It is found that the fraction of nanocrystals in the amorphous matrix may vary from 30 to 80% at different regimes of plasmochemical treatment [72].

A later study by the same authors [73] demonstrated a discrepancy between the F_{cr} values determined from CS spectra and X-ray findings. It should be borne in mind that the correct and representative evaluation of nanostructural parameters (grain size, distribution, etc.) need to be made by at least two and even three independent methods with subsequent thorough consideration of possible errors [3]. Therefore, many data obtained by either HRTEM, CS spectroscopy or X-ray analysis alone require correction.

Peculiarities of different methods for manufacturing nc-Si/a-Si composites are discussed in many publications (see Refs [15, 74 – 76]). High hydrogen solubility in Si nanocrystals distinguishes them as promising accumulators of hydrogen [77]. Theoretical estimation of stability of these nanocomposites based on molecular dynamic measurements was undertaken in [76]. Also, it was found that the critical radius of nanoparticles that can crystallize is ca. 1 nm [76].

In addition to [69, 71], detailed electron microscopic studies of hydrogen-containing semiconductor structures were carried out in [78, 79]. $Si_{0.69}Ge_{0.31}$ films (thickness 300 nm, grain size 45 nm) prepared by chemical precipitation during decomposition of a $SiH_2Cl_2 + GeH_4$ mixture ($T = 1070$ K) contained various defects (dislocations $a/6\{112\}$, asymmetric grain boundaries, twin lamellae, twins with 5-fold symmetry, etc.) [78]. It is unclear, however, whether these findings are universal, even though other authors also reported observation of twin structures. An HRTEM study using special techniques of spherical aberration and defocusing in 1.5 nm silicon nanocrystals revealed planar defects resembling twin boundaries and package defects [79]. Figure 10 shows a (111) twin boundary with atomic planes positioned at an angle of 70.5° on either side of it[1] and producing a moire contrast characteristic of high-resolution images. Such defects may be segregation sinks and show electric activity.

[1] This angle fairly well coincides with the theoretical value 70.53° characteristic of (111) twin boundaries in cubic structures.

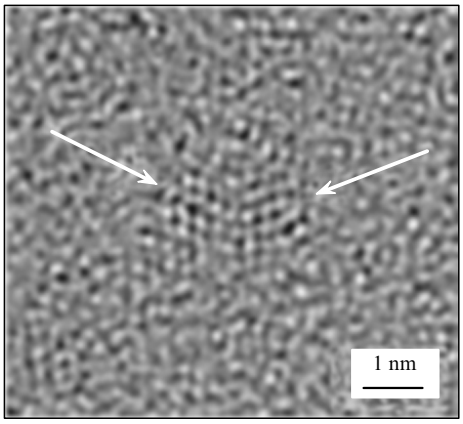

Figure 10. HRTEM image of a silicon crystallite in a nanocomposite film prepared by decomposition of an $He + H_2 + SiH_4$ mixture in a radio-frequency plasma [79].

3.2 Physical properties

Hydrogen admixtures in semiconducting nanostructures are attracting attention in the context of both the aforementioned fundamental problems related to nanocrystalline silicon and the technological aspects of other materials and their exploitation (light elements are present in the atmosphere of many technological processes). Different hydrogen behaviors in semiconductors may be illustrated by examples of silicon and germanium on the one hand and wide band-gap semiconductor zinc oxide on the other hand [80, 81]. In the former case, diffusion and solubility experiments demonstrate the atomic nature of hydrogen admixtures and their electric neutrality in tetrahedral positions. At the same time, hydrogen forms donor surface centers in ZnO, and hydrogen treatment significantly improves the electronic conductance of this oxide. Its thin films and fibers highly sensitive to hydrogen are considered promising for use in sensor devices. TiO_2 nanotubes are even more sensitive; their resistivity changes by almost 9 orders of magnitude after being held in nitrogen containing 1000 m.f. of hydrogen and air [82]. Such a prominent change is attributable to highly active states at the surface of nanotubes, their large specific surface, and perfect intertube contacts.

Semiconductors of other types also alter their properties under the action of hydrogen. For example, hydrogen treatment ($T = 470$ K, $t = 24$ h) of the surface of thin (Zn, Cd, Hg)Te films (narrow band-gap semiconductors) results in an appreciable change of their electric properties and in the appearance of photosensitivity [83]. Hydrogen initiates degradation of the electric parameters of GaInP/GaAs-based heteropolar transistors [84].

Many studies have investigated the effect of hydrogen on the volt – ampere characteristics of barrier nanostructures, such as palladium-semiconductor ones (Pd/GaAs/InGaAs, Pd/p-InGaAsP, Pd/n-InGaAs, Pd/porous GaAs, etc), designed for hydrogen detection (see, e.g., Refs [85 – 87]). Hydrogen was shown to affect volt – ampere characteristics, the response time, and direct and reverse currents as a result of adsorption of hydrogen atoms on the semiconductor surface, as well as a change in the electron work function [85]. Quantum wells increased sensitivity to hydrogen due to the formation of stress foci hampering migration of hydrogen into the bulk layers of GaAs [86].

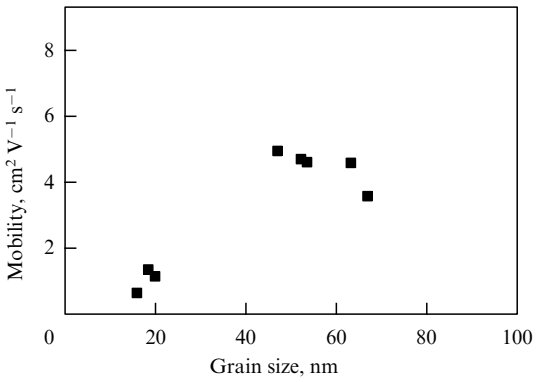

Figure 11. Grain size dependence of carrier mobility (direction ⟨220⟩) for an nc-Ge:H film obtained in an electron cyclotron resonance plasma [88].

The role of size effects in the formation of electric properties in Si and Ge-based nanostructured film composites was evaluated in [72, 88]. Comparison of nanocrystalline and interface fractions estimated from CS spectra of nc-Si:H films with the parameters of photoluminescence spectra suggests a marked influence of the interface (grain boundary) quality on the performance of silicon nanocomposites as materials for solar cells [72]. Figure 11 illustrates the effect of crystallite size on the Hall mobility of electrons in nanostructured germanium films. Also, the carrier concentration and mobility increased with increasing temperature [88]. The grain size dependence may be related to the scattering effect of the grains. The size effect on the carrier concentration is most likely due to different compositions of interfaces and grain bodies.

4. Insulators

4.1 General situation and selected fabrication methods

The article in *Nature* [89] in which the hydrogen storage capacity of single-wall carbon nanotubes was estimated at 5 – 10 mass% gave a powerful impetus to investigations of reversible hydrogen sorption by carbon nanostructures. Promising prospects for the application of fullerenes, single- and multiwall carbon nanotubes (CNTs) as hydrogen sorbents gave rise to hundreds of studies (see reviews [90 – 95]). The US Department of Energy established a minimal hydrogen content in hydrogen-accumulating structures (6.5 mass%) and did not consider grant applications for studies designed to work with lower concentrations.[2] However, further measurements revealed many errors in experiments using milligram quantities of inadequately inspected samples and the impossibility of reproducing many results. Today, the 'hydrogen – carbon' boom has abated, as appears from the materials of recent representative conferences [18, 19], and experiments are being carried out in a calmer atmosphere. Collective monograph [6] reports a more realistic sorption capacity of single- and multiwall CNTs at 77 – 300 K (under the hydrogen pressure up to 10 MPa). According to the majority of publications in 2000 – 2004, the currently achievable hydrogen content does not exceed 3 – 6 mass%. References [92 – 95] present comprehensive reviews of experimental and theoretical data on hydrogen-saturated carbon materials and the analysis of the reliability of the known sorption – desorption characteristics. The same reviews discuss the prospects of developing superadsorbents containing over 10 mass% H [95]. Taking these publications into account, what follows is focused on the structure and properties of hydrogen-saturated nanodielectrics.

Carbon nanostructures include single- and multiwall CNTs, fullerenes, nanofibers and their cords, nanoporous graphite, soot, diamond films, and nanodispersed diamond powders, also called detonation diamonds. It is appropriate to highlight certain methods for the production of fullerene-based hydrogen-containing substances (see [90] for details). The hydrogen (deuterium) pressure in manufacturing solid-phase hydrogen-containing fullerenes is normally 5 – 10 MPa ($T = 500 - 700$ K). Phases synthesized under such conditions have the composition $C_{60}H(D)_{24}$ or $C_{60}H(D)_{36}$ [90, 96, 97]. A higher saturation temperature may impoverish synthesized compositions (gas pressure 2.5 MPa) [98].

Deuteration temperature, K	623	673	723	773
Synthesized compound	$C_{60}D_{18.6}$	$C_{60}D_{29.3}$	$C_{60}D_{28.5}$	$C_{60}D_{27.5}$

On the other hand, prolonged saturation of fullerenes (500 h at 673 K and hydrogen pressure 1.2 MPa) results in their fragmentation.

A higher hydrogen content was reported in Refs [99 – 102] for hydration at high pressures created to decompose hydride phases (e.g., $AlH(D)_3$ or $LiAlH_4$) in heated copper ampules placed in a high-pressure apparatus. Specifically, graphite nanofibers 100 – 300 nm in diameter and single-wall CNTs treated with hydrogen at 10 GPa and 720 K contained 6.3 and 6.8 mass% H, respectively [100]. A two-step deuteration procedure (520 K, 21 h + 730 – 760 K, 9 h) of single-wall CNTs with the mean diameter ~ 1.5 nm at the pressure 5 GPa resulted in the deuterium content 10.8 ± 0.01 mass% [101]. Hydration of C_{60} at 2 GPa and 723 – 823 K was thoroughly investigated in [102]. Hydration proceeded very slowly at 723 K, whereas fullerenes disintegrated and released amorphous hydrogen at 800 K. The majority of experiments were carried out at 773 K for 30, 60, and 90 min. Hence, hydrogen interaction with C_{60} under high pressure and temperature may be described as fullerene polymerization at an earlier stage with the subsequent formation of $C_{60}H_x$-type compounds ($36 < x < 52$).

The attractive sorption characteristics of carbon nanostructures stimulated interest in the development of new nanocomposite materials, especially with the use of magnesium hydride (nanocomposites of the $MgH_2 - C$ type obtained by mechanosynthesis and subsequent hydration) (see, e.g., Refs [103 – 106]). The addition of carbon as graphite or nanofibers produces a positive effect on the sorption – desorption kinetics also apparent in films. But hydrogen content decreases, possibly due to the lowered amount of MgH_2 and formation of the amorphous phase. A nanocomposite based on magnesium hydride with an admixture of 5% $Ni/Al_2O_3/C$ containing ca. 5 mass% H was obtained by hydration at 9 MPa and room temperature over 6 h [106],

[2] Thereafter, this value was reduced to 6 mass%. Such hydrogen content in materials for its storage on board a vehicle is expected to be reached by 2010 as stipulated by the US Hydrogen program (9% in 2015) (http://www.eere.energy.gov/hydrogenandfuelcells/mypp).

supposedly due to reduced activation barriers and shorter diffusion paths in nanostructures.

4.2 Structural features and properties

A comprehensive comparative analysis of different approaches to the investigation of amorphous and nanocrystalline carbon materials exemplified by films (including hydrogen-containing ones) was made in [107]. Special attention was given to HRTEM, SEM, NMR, STM, AFM, CS and Auger spectroscopy, X-ray photoelectron spectroscopy (XPS), electron-energy-loss spectroscopy, and infrared spectroscopy (IRS).

Structural studies of fullerene hydrides by various methods (XSA, NMR, CS, and IR spectroscopy) have been reported by many authors (see Refs [90, 96–99]). For example, fullerene deuterides $C_{60}D_{24}$ (grain size 51–56 nm) and $C_{60}D_{36}$ were found to have an FCC lattice with the respective periods $a = 1.455$ nm and $a = 1.500$ nm. Diffractograms of samples obtained as described on p. 700 are presented in Fig. 12 [98]. It can be seen that the FCC lattice of the starting fullerene C_{60} was preserved after deuteration, but its period and volume increased as the peaks broadened. The crystallite (grain) size found from the half-width of the three most intense lines, (311), (220), and (111), proved to be 51–56 nm [96], i.e., within the generally accepted limit. An increase in the deuteration temperature led to progressive tailing and elimination of reflexes and the appearance of an amorphous halo at saturation temperatures above 723 and 773 K [98].

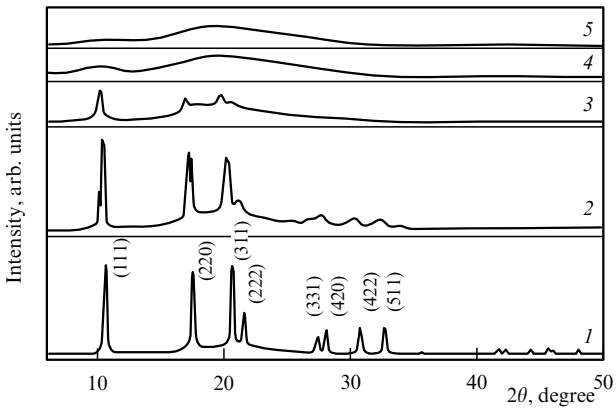

Figure 12. Diffractograms (CuK_α) of a starting fullerene before (*1*) and after deuteration at 623 (*2*), 673 (*3*), 723 (*4*), and 773 K (*5*) [98].

Fullerene hydrides like $C_{60}H_{36}$ have a BCC lattice with the period $a = 1.178$ nm [99]. Analysis of photoluminescence and IR spectra indicates that these compounds undergo phase transitions at ~ 0.7 and ~ 6 GPa.

NMR spectra of the type-$C_{60}H_{36}$ fullerene hydrides suggest the existence of isomers with different symmetries, i.e., a few types of hydrogen–carbon links [108–110]. For example, the T symmetry implies that all double bonds are localized in four isolated benzenoid rings on the surface of a fullerene molecule, at the vertices of an imaginary tetrahedron. The D_{3d} symmetry is characterized by the largest number of conjugated bonds in the poles of a molecule and along parallels. Examination of the electronic structure of hydrofullerene $C_{60}H_{36}$ by XPS, IRS, etc., combined with quantum-chemical computation also showed that the main spectral characteristics agree with calculations based on T- and D_{3d}-type symmetries [109–111]. A study of $C_{60}D_{24}$ demonstrated the presence of a small positive charge of deuterium atoms [96].

Isotopic and isomeric effects in fullerenes saturated with hydrogen and deuterium under high pressures (up to 3 GPa) were investigated based on their IR spectra that reflect molecular vibration patterns [112]. The IR spectra of fullerene hydrides and deuterides $C_{60}H_{36}$ and $C_{60}D_{36}$ exhibited multiple peaks produced by both partly reacted fullerenes and the aforementioned isomers. Different vibrational patterns of C–H and C–D bonds are described by the known relation $\Omega_H/\Omega_D \sim (M_{C_xH_y}/M_{C_xD_y})^{1/2}$, where $\Omega_{H,D}$ are the vibration frequencies and $M_{CH,CD}$ are the molecular weights of fullerene hydrides and deuterides. Table 3 shows the C–H and C–D vibration frequency ratios for some of the highest peaks of the IR spectrum. These data indicate that the highest ratios $(\Omega_H/\Omega_D)^2 \approx 1.73-1.79$ are close to the theoretical deuterium-to-hydrogen mass ratio equaling 2. Some peaks with low Ω considerably deviate from the theoretical value, suggesting a small contribution of bulk hydrogen and deuterium to these vibrations.

Table 3. Combination scattering frequencies of the highest peaks of fullerene hydride $C_{60}H_{36}$ and deuteride $C_{60}D_{36}$ [113].

$\Omega(C_{60}H_{36})$, cm^{-1}	$\Omega(C_{60}D_{36})$, cm^{-1}	Ω_H/Ω_D	$(\Omega_H/\Omega_D)^2$
206.6	203.4	1.016	1.032
212.4	209.7	1.013	1.020
464.2	464.4	1	1
484.4	484.4	1	1
2826.8	2113.6	1.337	1.789
2852.5	2169.7	1.315	1.728
2911.9	2209.3	1.318	1.737

Data on the physical properties of hydrogen nanodielectrics are rather scarce and await theoretical interpretation. Fullerene hydrides are reported to have the superconductivity and ferromagnetism properties [90, 109, 113], but they need to be studied in greater detail. The thermodynamic characteristics of $C_{60}H_{36}$ are known better than others: the heat capacity is in the 4.8–340 K range with calculated thermodynamic functions, vapor pressure, and sublimation enthalpy at $T = 550-680$ K, the standard enthalpy of formation [114–117]. Atomic vibrations make the largest contribution to the heat capacity of $C_{60}H_{36}$; the lattice contribution at room temperature is roughly an order of magnitude smaller [114]. Similar values of sublimation enthalpy calculated by the 2nd and 3rd thermodynamic laws from Knudsen data for vapor pressure suggest the reliability of the measurements [116]. Reaction enthalpy in the gaseous phase ($C_{60}H_{36} = C_{60} + 36\,H$) assessed from calorimetric findings for the enthalpy of formation equals 255.4 ± 0.8 kJ mol^{-1} per C–H bond, i.e., its absolute value is close to the analogous characteristics of other organic compounds like alkanes and cycloalkanes [117].

Other properties of hydrogen-containing nanodielectrics include the presence of hydrogen in thin amorphous alumina films responsible for a decrease in the elasticity and density moduli [118]. A study of hydrogen diffusion in diamond films with the grain size 200–1000 nm (including those doped with boron up to $10^{19}-10^{20}$ cm^{-3}) suggests an important role of the hydrogen capture by defects at intergranular interfaces [119]. An increased hydrogen content in thin amorphous carbon films is associated with their decreased roughness, enhanced hardness, and higher elasti-

city modulus. [120]. Quantum-chemical analysis [123] of hydrogen-saturated boron hydride nanotubes considered in Refs [121, 122] implies formation of structures with new physical properties, such as dielectric – semiconductor and dielectric – metal.

It is worthwhile mentioning a large number of theoretical works within different approximations (Monte Carlo, molecular dynamics, density functional methods, etc.) for calculation of the electron structure of carbon and other hydrogen-saturated nanotubes (see [111, 123 – 128] and the relevant references in reviews [90 – 95]). Discussion of these results is beyond the scope of this paper and needs special consideration. The same refers to the results of recent calculations in Refs [129 – 131]. It is assumed that a fullerene surface may be used to symmetrically arrange complexes such as $C_{60}[ScH_2]_{12}$ or $C_{48}B_{12}[ScH_2]_{12}$, capable of reversible hydrogen sorption at the respective rates of 7 and 8.77 mass% [129]. Similarly, the surfaces of C_{60} and single-wall CNTs can be decorated with light transition metal atoms binding molecular hydrogen (up to four H_2 molecules in the case of Ti) [130, 131]. It is supposed that desorption will proceed at room temperature.

We note that templates or matrices (fullerene and nanotube surfaces as in [129 – 131]) are widely used for 'nanopositioning' the desired atomic groups in modern catalytic and other nanomaterials [1 – 6]. Further in-depth experimental studies should confirm the reality of predictions [129 – 131] and arguments [132] in favor of the high sorption capacity of carbine layers and graphite foams. 'Computational synthesis' of hydrogen nanostructures and prognostic estimation of their properties based on comprehensive information about their electron structure may significantly promote the development of totally new nanomaterials with predetermined physical and chemical properties.

5. Conclusion

This review is confined to the consideration of experimental data on hydrogen nanostructures. As mentioned above, many questions remain to be elucidated, despite the rather wide spectrum of ongoing studies. More information is needed on size-related effects, mechanisms of stability, and reproducibility of hydrogen nanostructures, as well as the development of novel methods for their theoretical description, and reliable and cost-effective regimes for their fabrication with a high attestation level. These problems are applicable to many nanostructured materials [3]. It is equally clear that further in-depth studies of hydrogen nanostructures will contribute to their extensive practical application, not only in hydrogen energetics, nanoelectronics, and the construction of sensor systems but also in the development of nanomineralogical ideas pertaining to the origin of the earth's crust and the search for mineral deposits [133].

The author thanks his colleagues E F Shek, I O Bashkina, A S Lobacheva, and Yu M Shul'ga for discussions of this review and the opportunity to look through publications. Thanks are also due to the Russian Foundation for Basic Research for its support (grant 06-03-07009).

References

1. Roco M K, Williams R S, Alivisatos P (Eds) *Nanotechnology Research Directions*: *IWGN Workshop Report*: *Vision for Nanotechnology in the Next Decade* (Dordrecht: Kluwer Acad. Publ., 2000) [Translated into Russian (Moscow: Mir, 2002)]
2. Pool C P (Jr.), Owens F J *Introduction to Nanotechnology* (Hoboken, NJ: J. Wiley, 2003) [Translated into Russian (Moscow: Tekhnosfera, 2004)]
3. Andrievskii R A, Ragulya A V *Nanostructurnye Materialy* (Nanostructured Materials) (Moscow: Akademiya, 2005)
4. Gusev A I *Nanomaterialy, Nanostruktury, Nanotekhnologii* (Nanomaterials, Nanostructures, Nanotechnologies) (Moscow: Fizmatlit, 2005)
5. Suzdalev I P *Nanotekhnologiya. Fiziko-Khimiya Nanoklasterov, Nanostruktur i Nanomaterialov* (Nanotechnology. Physico-Chemistry of Nanoclusters, Nanostructures, and Nanomaterials) (Moscow: KomKniga, 2006)
6. Gogotsi Yu (Ed.) *Nanomaterials Handbook* (Boca Raton, Fl.: CRC Press/Taylor & Francis, 2006)
7. Mueller W M, Blackledge J P, Libowitz G G (Eds) *Metal Hydrides* (New York: Academic Press, 1968) [Translated into Russian (Moscow: Atomizdat, 1973)]
8. Bashkin I O, Ponyatovskii E G *Materialovedenie* (2) 35 (1997)
9. Alefeld G, Völkl J (Eds) *Hydrogen in Metals* Vol. 1, 2 (Berlin: Springer-Verlag, 1978) [Translated into Russian (Moscow: Mir, 1981)
10. Andrievskii R A *Materialovedenie Gidridov* (Science of Hydrids) (Moscow: Metallurgiya, 1986)
11. Maksimov E G, Pankratov O A *Usp. Fiz. Nauk* **116** 385 (1975) [*Sov. Phys. Usp.* **18** 481 (1975)]
12. Andrievskii R A, Umanskii Ya S *Fazy Vnedreniya* (Introduction Phases) (Moscow: Nauka, 1977)
13. Gel'd P V, Ryabov R A, Mokhracheva L P *Vodorod i Fizicheskie Svoistva Metallov i Splavov*: *Gidridy Perekhodnykh Metallov* (Hydrogen and Physical Properties of Metals and Alloys: Transition Metal Hydrides) (Moscow: Nauka, 1985)
14. Nazri G-A et al. (Eds) *Hydrogen Storage Materials* (MRS Symp. Proc., Vol. 801) (Warrendale, PA: MRS, 2004)
15. Ganguly G et al. (Eds) *Amorphous and Nanocrystalline Silicon Science and Technology — 2004* (MRS Symp. Proc., Vol. 808) (Warrendale, PA: MRS, 2004)
16. Heben M J et al. (Eds) *Materials for Hydrogen Storage — 2004* (MRS Symp. Proc., Vol. 837) (Warrendale, PA: MRS, 2005)
17. Nazri G-A et al. (Eds) *Materials and Technology for Hydrogen Storage and Generation* (MRS Symp. Proc., Vol. 884E) (Warrendale, PA: MRS, 2005)
18. Figiel H, Zogal O J, Yartys V (Eds) *Proc. of the 9th Intern. Symp. on Metal – Hydrogen Systems, Fundametals and Applications (MH2004), Cracow, Poland, 5 – 10 September 2004*; *J. Alloys Comp.* **404 – 406** (2005)
19. Veziroglu T N et al. (Eds) *Hydrogen Materials Science and Chemistry of Carbon Nanomaterials* (Berlin: Springer, 2007)
20. Mesyats G A, Prokhorov M D *Vestn. Ross. Akad. Nauk* **74** 579 (2004) [*Herald Russ. Acad. Sci.* **74** 377 (2004)]
21. Kostanchuk I G, Ivanov V Yu, Boldyrev V V *Dokl. Akad. Nauk SSSR* **286** 385 (1986)
22. Zaluski L, Zaluska A, Ström-Olsen J O *J. Alloys Comp.* **217** 245 (1995)
23. Janot R et al. *Intermetallics* **14** 163 (2006)
24. Doppiu S et al. *J. Alloys Comp.* **404 – 406** 27 (2005)
25. Friedrichs O et al. *Acta Mater.* **54** 105 (2006)
26. Varin R A, Czujko T, Wronski Z *Nanotechnology* **17** 3856 (2006)
27. Ueda T T et al. *J. Alloys Comp.* **386** 253 (2005)
28. Singh S K et al. *Int. J. Hydrogen Energy* **14** 573 (1989)
29. Andrievskii R A *Usp. Khim.* **66** 57 (1997) [*Russ. Chem. Rev.* **66** 53 (1997)]
30. Korobov I I et al. *Elektrokhimiya* **34** 1508 (1998) [*Russ. J. Electrochem.* **34** 1365 (1998)]
31. Andrievskii R A *Nanostrukturnoe Materialovedenie* (3) 41 (2005)
32. Ouyang L Z et al. *J. Alloys Comp.* **404 – 406** 485 (2005)
33. Vredenberg A M, Heller E M B, Boerma D O *J. Alloys Comp.* **400** 188 (2005)
34. Vargas W E et al. *Thin Solid Films* **496** 189 (2006)
35. Paillier J, Roue L *J. Alloys Comp.* **404 – 406** 473 (2005)
36. Ingason A S, Olafsson S *J. Alloys Comp.* **404 – 406** 469 (2005)
37. Pundt A et al. *Mater. Sci. Eng. B* **108** 19 (2004)
38. Shao H et al. *Mater. Sci. Eng. B* **110** 221 (2004)
39. Itoh K et al. *J. Alloys Comp.* **404 – 406** 95 (2005)

40. Fukunaga T et al. *Mater. Sci. Eng. B* **108** 105 (2004)
41. Rush J J, Rowe J M, Maeland A J *J. Phys. F: Met. Phys.* **10** L283 (1980)
42. Hanneken J W et al. *J. Alloys Comp.* **330–332** 714 (2002)
43. Au M *Mater. Sci. Eng. B* **117** 37 (2005)
44. De Veirman A E M, Staals A A, Notten P H L *Philos. Mag. A* **70** 837 (1994)
45. Kim G-H et al. *Acta Metall. Mater.* **43** 2233 (1995)
46. Ares J R, Cuevas F, Percheron-Guégan A *Acta Mater.* **53** 2157 (2005)
47. Nechaev Yu S *Usp. Fiz. Nauk* **171** 1251 (2001) [*Phys. Usp.* **44** 1189 (2001)]
48. Pundt A, Kirchheim R *Annu. Rev. Mater. Res.* **36** 555 (2006)
49. Zaluski L et al. *J. Mater. Sci.* **31** 695 (1996)
50. Kuji T et al. *J. Alloys Comp.* **330–332** 718 (2002)
51. Andrievski R A et al. *Int. J. Hydrogen Energy* **21** 949 (1996)
52. Swalin R A *Thermodynamics of Solids* (New York: Wiley, 1962) [Translated into Russian (Moscow: Metallurgiya, 1968)]
53. Eliaz N, Eleizer D *Adv. Perform. Mater.* **6** 5 (1999)
54. Gapontsev A V, Kondrat'ev V V *Usp. Fiz. Nauk* **173** 1107 (2003) [*Phys. Usp.* **46** 1077 (2003)]
55. Mütschele T, Kirchheim R *Scripta Metall.* **21** 135 (1987)
56. Gapontsev A V, Kondrat'ev V V, in *Nanotekhnologiya i Fizika Funktsional'nykh Nanokristallicheskikh Materialov* (Nanotechnology and Physics of Functional Nanocrystalline Materials) Vol. 2 (Eds V V Ustinov, N I Noskova) (Ekaterinburg: UrO RAN, 2005) p. 84
57. Yamakawa K et al. *J. Alloys Comp.* **393** 5 (2005)
58. Huiberts J N et al. *Nature* **380** 231 (1996)
59. Sakaguchi H et al. *J. Less-Common Met.* **135** 137 (1987)
60. Singh M *Int. J. Hydrogen Energy* **21** 223 (1996)
61. Devi B, Banthia A S, Jain I P *Int. J. Hydrogen Energy* **29** 1289 (2004)
62. Slack J L et al. *Solar Energy Mater. Solar Cells* **90** 485 (2006)
63. Zaikov N K et al. *Fiz. Tverd. Tela* **39** 908 (1997) [*Phys. Solid State* **39** 810 (1997)]
64. Mushnikov N V et al. *J. Alloys Comp.* **292** 51 (1999)
65. Sinning H-R, Golovin I S *J. Alloys Comp.* **404–406** 519 (2005)
66. Longeaud C et al. *J. Non-Cryst. Solids* **227–230** 96 (1998)
67. Afanas'ev V P et al. *Fiz. Tekh. Poluprovodn.* **34** 492 (2000) [*Semicond.* **34** 477 (2000)]
68. Golikova O A *Fiz. Tekh. Poluprovodn.* **36** 730 (2002) [*Semicond.* **36** 691 (2002)]
69. Vallat-Sauvain E et al. *J. Appl. Phys.* **87** 3137 (2000)
70. Wyrsh N et al., in *Amorphous and Heterogeneous Silicon Thin Films — 2000* (MRS Symp. Proc., Vol. 609, Eds R W Collins et al.) (Warrendale, PA: MRS, 2000) A15.1.1
71. Tyschenko I E et al. *Fiz. Tekh. Poluprovodn.* **38** 111 (2004) [*Semicond.* **38** 107 (2004)]
72. Wang K et al., in *Amorphous and Nanocrystalline Silicon Science and Technology — 2004* (MRS Symp. Proc., Vol. 808, Eds G Ganguly et al.) (Warrendale, PA: MRS, 2004) A9.53.1
73. Wang K et al., in *Amorphous and Nanocrystalline Silicon Science and Technology — 2005* (MRS Symp. Proc., Vol. 862, Eds R W Collins et al.) (Warrendale, PA: MRS, 2005) A10.2.1
74. Naumova O V et al. *Fiz. Tekh. Poluprovodn.* **37** 93 (2003) [*Semicond.* **37** 92 (2003)]
75. Afanas'ev V P et al. *Fiz. Tekh. Poluprovodn.* **38** 226 (2004) [*Semicond.* **38** 221 (2004)]
76. Biswas R, Pan B C, Selvaraj V, in *Amorphous and Nanocrystalline Silicon Science and Technology — 2005* (MRS Symp. Proc., Vol. 862, Eds R W Collins et al.) (Warrendale, PA: MRS, 2005) A24.3.1
77. Neiner D et al., in *Hydrogen Storage Materials, Symp. EE, April 17–20, 2006* (Warrendale, PA: MRS, 2006) EE3.19
78. Qin W, Ast D G, Kamins T I, in *Amorphous and Heterogeneous Silicon Thin Films — 2000* (MRS Symp. Proc., Vol. 609, Eds R W Collins et al.) (Warrendale, PA: MRS, 2000) A8.4.1
79. Perrey C R, Thompson S S, Lentzen M, in *Amorphous and Nanocrystalline Silicon Science and Technology — 2004* (MRS Symp. Proc., Vol. 808, Eds G Ganguly et al.) (Warrendale, PA: MRS, 2004) A8.7.1
80. Haller E E, in *Hydrogen in Semiconductors* (MRS Symp. Proc., Vol. 813, Eds N H Nickel, M D McCluskey, S Zhang) (Warrendale, PA: MRS, 2004) H1.1.1/A1.1.1
81. McCluskey M D, Jokela S J, Hlaing O W M *Physica B* **376–377** 690 (2006)
82. Paulose M et al. *Nanotechnology* **17** 398 (2006)
83. Khlyap G M, Sydorchuk P G, in *Hydrogen in Semiconductors* (MRS Symp. Proc., Vol. 813, Eds N H Nickel, M D McCluskey, S Zhang) (Warrendale, PA: MRS, 2004) H4.3.1
84. Tartarin J G et al., in *Hydrogen in Semiconductors* (MRS Symp. Proc., Vol. 813, Eds N H Nickel, M D McCluskey, S Zhang) (Warrendale, PA: MRS, 2004) H4.1.1
85. Voronkov V P, Khludkova L S *Fiz. Tekh. Poluprovodn.* **33** 1220 (1999) [*Semicond.* **33** 1111 (1999)]
86. Karpovich I A et al. *Fiz. Tekh. Poluprovodn.* **36** 582 (2002) [*Semicond.* **36** 552 (2002)]
87. Salehi A, Nikfarjam A, Kalantari D J *Sensors Actuators B: Chem.* **113** 419 (2006)
88. Niu X, Booher J, Dalal V L, in *Amorphous and Nanocrystalline Silicon Science and Technology — 2005* (MRS Symp. Proc., Vol. 862, Eds R W Collins et al.) (Warrendale, PA: MRS, 2005) A10.2.1
89. Dillon A C et al. *Nature* **386** 377 (1997)
90. Tarasov B P, Gol'dshleger N F, Moravsky A P *Usp. Khim.* **70** 149 (2001) [*Russ. Chem. Rev.* **70** 131 (2001)]
91. Züttel A et al. *Mater. Sci. Eng. B* **108** 9 (2004)
92. Eletskiĭ A V *Usp. Fiz. Nauk* **174** 1191 (2004) [*Phys. Usp.* **47** 1119 (2004)]
93. Nechaev Yu S, Alekseeva O K *Usp. Khim.* **73** 1308 (2004) [*Russ. Chem. Rev.* **73** 1211 (2004)]
94. Nechaev Yu S *Materialovedenie* (2) 16 (2006)
95. Nechaev Yu S *Usp. Fiz. Nauk* **176** 581 (2006) [*Phys. Usp.* **49** 563 (2006)]
96. Shul'ga Yu M et al. *Fiz. Tverd. Tela* **41** 1520 (1999) [*Phys. Solid State* **41** 1391 (1999)]
97. Talyzin A V, Shulga Y M, Jacob A *Appl. Phys. A* **78** 1005 (2004)
98. Shul'ga Y M et al. *Carbon* **41** 1365 (2003)
99. Meletov K P et al. *Fiz. Tverd. Tela* **44** 519 (2002) [*Phys. Solid State* **44** 542 (2002)]
100. Bashkin I O et al. *Pis'ma Zh. Eksp. Teor. Fiz.* **79** 280 (2004) [*JETP Lett.* **79** 226 (2004)]
101. Shul'ga Yu M et al. *Pis'ma Zh. Eksp. Teor. Fiz.* **80** 884 (2004) [*JETP Lett.* **80** 752 (2004)]
102. Talyzin A V et al. *Chem. Phys.* **325** 445 (2006)
103. Imamura H et al. *Acta Mater.* **51** 6407 (2003)
104. Klyamkin S N et al. *Al'ternativnaya Energetika Ekologiya* **4** (1) 5 (2005) [*Int. Sci. J. Alternative Energy Ecology* (1) 27 (2005)]
105. Kojima Y, Kawai Y, Haga T, in *Materials for Hydrogen Storage — 2004* (MRS Symp. Proc., Vol. 837, Eds M J Heben et al.) (Warrendale, PA: MRS, 2005) N3.5.1
106. Rougier A et al., in *Materials and Technology for Hydrogen Storage and Generation* (MRS Symp. Proc., Vol. 884E, Eds G-A Nazri et al.) (Warrendale, PA: MRS, 2005) GG6.1.1
107. Chu P K, Li L *Mater. Chem. Phys.* **96** 253 (2006)
108. Lobach A S et al. *Izv. Ross. Akad. Nauk Ser. Khim.* (4) 671 (1997) [*Russ. Chem. Bull.* **46** 641 (1997)]
109. Lobach A S et al. *Fuller. Sci. Technol.* **6** 375 (1998)
110. Tarasov V P et al. *Appl. Phys. A* **78** 1001 (2004)
111. Okotrub A V et al. *Zh. Neorg. Khim.* **45** 523 (2000) [*Russ. J. Inorg. Chem.* **45** 457 (2000)]
112. Meletov K P et al. *Chem. Phys.* **263** 379 (2001)
113. Shul'ga Yu M et al. *Zh. Fiz. Khim.* **72** 115 (1998) [*Russ. Phys. Chem.* **72** 103 (1998)]
114. Lebedev B V, Bykova T A, Lobach A S *Dokl. Ross. Akad. Nauk* **368** 629 (1999) [*Dokl. Chem.* **368** 237 (1999)]
115. Lebedev B V, Bykova T A, Lobach A S *J. Therm. Anal. Calor.* **62** 257 (2000)
116. Dorozhko P A et al. *Chem. Phys. Lett.* **336** 39 (2001)
117. Pimenova S M et al. *J. Phys. Chem. B* **106** 2127 (2002)
118. Schneider J M et al. *Appl. Phys. Lett.* **80** 1144 (2002)
119. Ballutaud D et al., in *Hydrogen in Semiconductors* (MRS Symp. Proc., Vol. 813, Eds N H Nickel, M D McCluskey, S Zhang) (Warrendale, PA: MRS, 2004) H8.3.1
120. Fang T-H, Chang W-J *Appl. Surf. Sci.* **252** 6243 (2006)
121. Tang C et al. *J. Am. Chem. Soc.* **124** 14550 (2002)
122. Ma R et al. *Appl. Phys. Lett.* **81** 5225 (2002)

123. Lebedev N G, Zaporotskova I V, Chernozatonskii L A *Khim. Fiz.* **25** (8) 77 (2006)
124. Lebedev N G, Zaporotskova I V, Chernozatonskii L A *Int. J. Quantum Chem.* **96** 142 (2004)
125. Zaporotskova I V *Nanotekhnika* (4) 73 (2005)
126. Cabria I, López M J, Alonso J A *Comput. Mater. Sci.* **35** 238 (2006)
127. Ren Y X, Ng T Y, Liew K M *Carbon* **44** 397 (2006)
128. Sheka E F *Zh. Strukt. Khim.* **47** 613 (2006) [*J. Struct. Chem.* **47** 593 (2006)]
129. Zhao Y et al. *Phys. Rev. Lett.* **94** 155504 (2005)
130. Yildirim T, Ciraci S *Phys. Rev. Lett.* **94** 175501 (2005)
131. Yildirim T, Iñiguez J, Ciraci S *Phys. Rev. B* **72** 153403 (2005)
132. Patchkovskii S et al. *Proc. Natl. Acad. Sci. USA* **102** 10439 (2005)
133. Yushkin N P, Askhabov A M, Rakiv V I (Executive Eds) *Nanomineralogiya. Ul'tra i Mikrodispersnoe Sostoyanie Mineral'nogo Veshchestva* (Nanomineralogy. Ultra and Microdospersed State of Mineral Matter (St. Petersburg: Nauka, 2005)